

This document is confidential and is proprietary to the American Chemical Society and its authors. Do not copy or disclose without written permission. If you have received this item in error, notify the sender and delete all copies.

**Capturing Plasmon-Molecule Dynamics in Dye Monolayers
on Metal Nanoparticles using Classical Electrodynamics with
Quantum Embedding**

Journal:	<i>The Journal of Physical Chemistry</i>
Manuscript ID	jp-2017-03440v
Manuscript Type:	Article
Date Submitted by the Author:	11-Apr-2017
Complete List of Authors:	Smith, Holden; Louisiana State University, Department of Chemistry Karam, Tony; California Institute of Technology, Chemistry Haber, Louis; Louisiana State University, Department of Chemistry Lopata, Kenneth; Louisiana State University, Chemistry

SCHOLARONE™
Manuscripts

Capturing Plasmon-Molecule Dynamics in Dye Monolayers on Metal Nanoparticles using Classical Electrodynamics with Quantum Embedding

Holden T. Smith,[†] Tony E. Karam,^{†,¶} Louis H. Haber,[†] and Kenneth Lopata^{*,†,‡}

Department of Chemistry, Louisiana State University, Baton Rouge, LA 70803, and Center for Computation & Technology, Louisiana State University, Baton Rouge, LA 70803

E-mail: klopata@lsu.edu

*To whom correspondence should be addressed

[†]Department of Chemistry, Louisiana State University, Baton Rouge, LA 70803

[‡]Center for Computation & Technology, Louisiana State University, Baton Rouge, LA 70803

[¶]Arthur Amos Noyes Laboratory of Chemical Physics, California Institute of Technology, Pasadena, CA 91125

Abstract

A multi-scale hybrid quantum/classical approach using classical electrodynamics and a collection of discrete three-level quantum systems is used to simulate the coupled dynamics and spectra of a malachite green monolayer adsorbed to the surface of a spherical gold nanoparticle (NP). This method utilizes finite difference time domain (FDTD) to describe the plasmonic response of the NP within the main FDTD framework and a three-level quantum description for the molecule via a Maxwell/Liouville framework. To avoid spurious self-excitation, each quantum molecule has its own auxiliary FDTD subregion embedded within the main FDTD grid. The molecular parameters are determined by fitting the experimental extinction spectra to Lorentzians, yielding the energies, transition dipole moments, and the dephasing lifetimes. This approach is suited to modeling thousands of molecules on the surface of a plasmonic NP. There is good agreement with experimental extinction measurements, predicting the plasmon and molecule depletions. Additionally, this model captures the polariton peaks overlapped with a Fano-type resonance profile observed in the experimental extinction measurements. This technique can be generalized to any nanostructure/multi-chromophore system, where the molecules can be treated with essentially any quantum method.

Keywords

plasmons, polaritons, Fano resonance, quantum/classical modeling, electrodynamics, quantum mechanics, finite-difference time-domain

1 Introduction

Noble metal nanoparticles (NPs) possess unique chemical, electronic, and optical properties with important applications spanning molecular sensing, catalysis, metamaterials, and biologically-relevant technologies.^{1–10} Many of these applications exploit field enhancements

1
2
3 due to localized surface plasmon resonances, which are coherent oscillations of the free
4 electrons at the NPs surface.^{11–14} Changing the composition, size, shape, and surround-
5 ing medium allows for tunable optical properties of these plasmonic NPs. These broadly
6 tunable NPs show promise for the molecular detection, metamaterials, and novel dispersion
7 properties.¹⁵ Plasmonic gold and silver nanoparticles can be functionalized with biological
8 molecules and polymers through thiolation for applications in biolabeling,^{16,17} drug deliv-
9 ery,^{11,18} and photothermal therapy.^{19–21}

12 Nonlinear responses of plasmonic nanoparticles such as second harmonic generation
13 (SHG) and sum frequency generation (SFG) can be significantly enhanced due to these
14 plasmon resonances.^{22–29} Additionally, interactions between plasmonic nanoparticles and
15 chromatic dyes give rise to molecular and plasmonic resonance coupling, which can be mea-
16 sured via extinction spectroscopy. When the plasmon frequency is in resonance with a
17 molecular excitation, strong coupling can lead to the formation of hybrid states, resulting
18 in exciton-polariton peaks separated by a splitting energy. Additionally, this coupling leads
19 to characteristic Fano-type resonances with corresponding plasmon and molecular spectral
20 depletions.^{30–32,32–38}

23 The near-field dynamics and coupled dynamics of molecules, such as light harvesting
24 dyes adsorbed to the surface of plasmonic nanostructures,¹¹ show promise in the fields of
25 photovoltaics, catalysis, and chemical sensing. For example, the strong fields near the sur-
26 face of metal nanoparticles can boost the response of nearby adsorbates in low concentra-
27 tions which is ideal for sensing applications such as surface enhanced Raman spectroscopy
28 (SERS), or conversely, the optical responses of molecules at the surface of metallic nanos-
29 tructures can induce plasmonic modes via surface-enhanced fluorescence. There has been
30 much recent progress towards modeling these hybrid molecular/plasmonic systems. Some
31 of the many approaches to model the dynamics between plasmons and molecules include
32 point-plasmon/random phase approximation (RPA),^{39,40} time-dependent density functional
33 theory (TDDFT) with small metal clusters,^{41,42} coupled Liouville/Maxwell equations,⁴³ elec-

trodynamics coupled to a density matrix master equation,³³ and quantum electrodynamics coupled with time-dependent Hartree-Fock.³²

Quantum/classical approaches based on a finite-difference time-domain (FDTD) solution to Maxwell's equations, with embedded quantum oscillators, are especially versatile as they can describe arbitrary geometries of nanostructures with a nearby quantum emitter (e.g., molecule or quantum dot), potentially with solvent effects included. Typically these approaches involve a single quantum point source, but in many real systems there is coupling between nanoparticles (NPs) and thousands of nearby dyes (e.g., adsorbed on the surface). This requires an extensible approach capable of describing an arbitrary number of quantum sub-regions within the FDTD main grid. In this paper, we present a method for simulating thousands of molecules on the surface of a spherical, plasmonic nanoparticle and compare these results to experimental extinction measurements. We use a phenomenological N -level Hamiltonian for each molecule, but this approach can be extended to accommodate any quantum description.

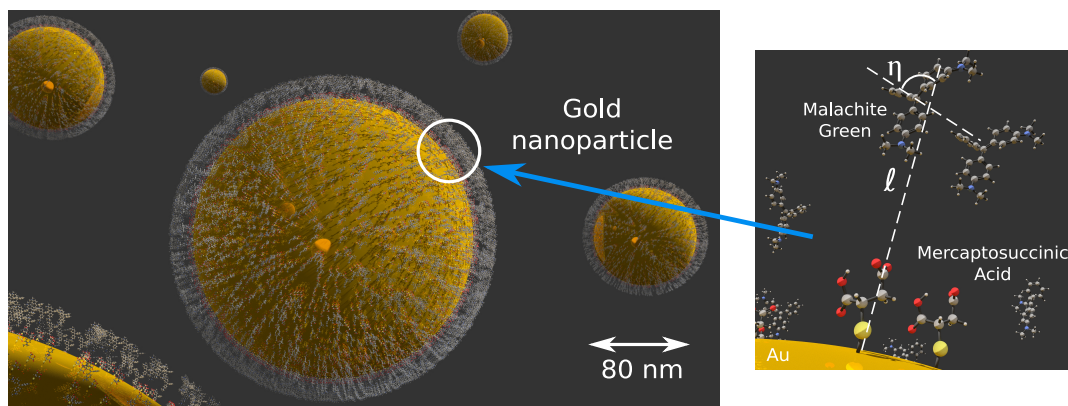


Figure 1: Schematic of the gold/dye interface. The cationic malachite green (MG) molecules are held at the surface via electrostatic interactions with the anionic mercaptosuccinic acid (MSA) with a small water solvation layer between the MG and MSA. The transition dipole moment for the brightest absorption is tilted with respect to the normal of the surface by angle η . Assuming roughly two water shells, the overall separation ℓ between the Au surface and the MG center of mass is roughly 25.4 Å.

The remainder of the paper is structured as follows: In Sec. 2, we present expressions for

the FDTD evolution of the electric fields, magnetic fields, currents and polarizations for a combined plasmon/molecule system, followed by an explanation of how to implement a combined FDTD/ N -level approach. Sec. 3 presents validation simulations including: single gold NP extinction spectra, long-range resonant energy transfer (FRET) between two molecules, and finally difference extinction spectra for malachite green monolayers adsorbed on a Au NP (See Fig. 1). Comparison of these spectra with experiment allows us to extract approximate transition dipole angles and monolayer separation distances. Finally, conclusions and future extensions are presented in Sec. 4.

2 Theory

In this section, we outline an approach for coupling multiple quantum oscillators within a classical electrodynamics background described using FDTD. Broadly, this involves five components:

1. Describe the electric and magnetic fields in the vacuum (or background medium), and the fields and currents on the metal nanoparticle, using FDTD.
2. Partition an auxiliary FDTD subregion around each quantum oscillator (molecule) to remove spurious self-excitation of the molecules with their radiated fields. This uses a total-field/scattered-field (TFSF) approach.
3. Propagate each quantum molecule in time under the influence of the external field from the FDTD. This can be done using any quantum method, but here we use phenomenological N -level molecules.
4. The quantum currents on each molecule act as source terms for the main FDTD grid via the TFSF boundary around each molecular subregion.

2.1 Basic FDTD Considerations

In the finite-difference time-domain (FDTD) approach, the fields and currents are discretized on a grid and solved in time and space using a “leap-frog” integrator.⁴⁴ The spatial and frequency-dependent permittivity $\varepsilon(r)$ and permeability, $\mu(r)$ are typically fit to experimental bulk values, which makes FDTD a semi-empirical method. Neglecting magnetization effects in the metal (i.e., $\mu = \mu_0$), the Maxwell’s equations are:

$$\varepsilon_{\text{eff}}(\mathbf{r}) \frac{\partial}{\partial t} \mathbf{E}(\mathbf{r}, t) = \nabla \times \mathbf{H}(\mathbf{r}, t) - \mathbf{J}(\mathbf{r}, t) \quad (1a)$$

$$\mu_0 \frac{\partial}{\partial t} \mathbf{H}(\mathbf{r}, t) = -\nabla \times \mathbf{E}(\mathbf{r}, t) \quad (1b)$$

where $\mathbf{E}(\mathbf{r}, t)$ is the electric field, $\mathbf{H}(\mathbf{r}, t)$ is the magnetic field, and $\mathbf{J}(\mathbf{r}, t)$ is the electric current density. Note that in this paper, \mathbf{J} is only present on the metal nanostructure.

To avoid issues with “hard sources,” where propagated fields interact in non-physical ways with the source, we use a total-field scattered-field (TF-SF) approach.^{45–47} Here, an auxiliary 1D simulation with a specified pulse is propagated separately from the main 3D grid. The 1D incident field is added uniformly to the “left” TFSF boundary of the 3D grid, and subtracted out on the “right”. By subtracting the incident field, the resulting simulation outside the total-field region contains only scattered fields. This technique is commonly used to calculate the scattering cross sections of arbitrary objects via the outgoing flux (outside the TFSF) along with a near-to-far-field transform (NTFF).⁴⁸ The corresponding absorption cross section can be computed inside the TF region using flux monitors, but this approach can be somewhat sensitive to monitor position and grid spacing. Details on calculating the absorption and scattering cross sections are outlined in the Supporting Information.

2.2 Coupling between Quantum Mechanics and FDTD

The electron dynamics in molecules must be described using quantum mechanics, which necessitates a multiscale coupling between the main FDTD grid and multiple quantum sub-regions. For simplicity, we assume that each molecule only occupies one grid point. Thus, the FDTD electric field at that point acts as an external field on the molecule, and the molecular current acts as a source for the FDTD. Direct application of this, however, results in spurious self-excitation of the molecule, as the radiated field can immediately “re-excite” the emitting molecule. One way of overcoming this is to use a full auxiliary FDTD grid for each molecule,⁴⁰ but this is not tractable for a large number of molecules. A better alternative is to instead partition a small FDTD region around each molecule using a TFSF-like coupling, such as the approach developed by Seideman and coworkers.⁴³ By propagating this fields in this small region using the analytical expression for a radiating dipole, the radiated fields from the molecule do not interact with the molecule itself, but are instead coupled back into the main grid some distance away using a “reverse” TFSF boundary. In this paper we instead propagate using a FDTD with a point source, which is valid for any quantum emitter.

Fig. 2 shows a schematic of the approach for the case of two molecules. The main FDTD has two regions: a total field (TF) region which contains all nanostructures and molecules, and a scattered field (SF) region which contains only the scattered fields (i.e., no incident pulse). The boundary of the main FDTD region was taken to be a second-order Mur absorbing boundary to remove non-physical reflections.⁴⁶ The system is excited with a broadband pulse via the TFSF interface, as described in the previous section. This electric field then acts as an external applied source for each quantum molecule in the region. Rather than radiate back into the TF region, which would allow the molecule to nonphysically excite itself, instead each molecule radiates into its own auxiliary FDTD region centered around the molecule (see Fig. 2). After propagating some distance from the molecule, this molecular field is then added back to the main FDTD grid via a “reverse” TFSF boundary. These

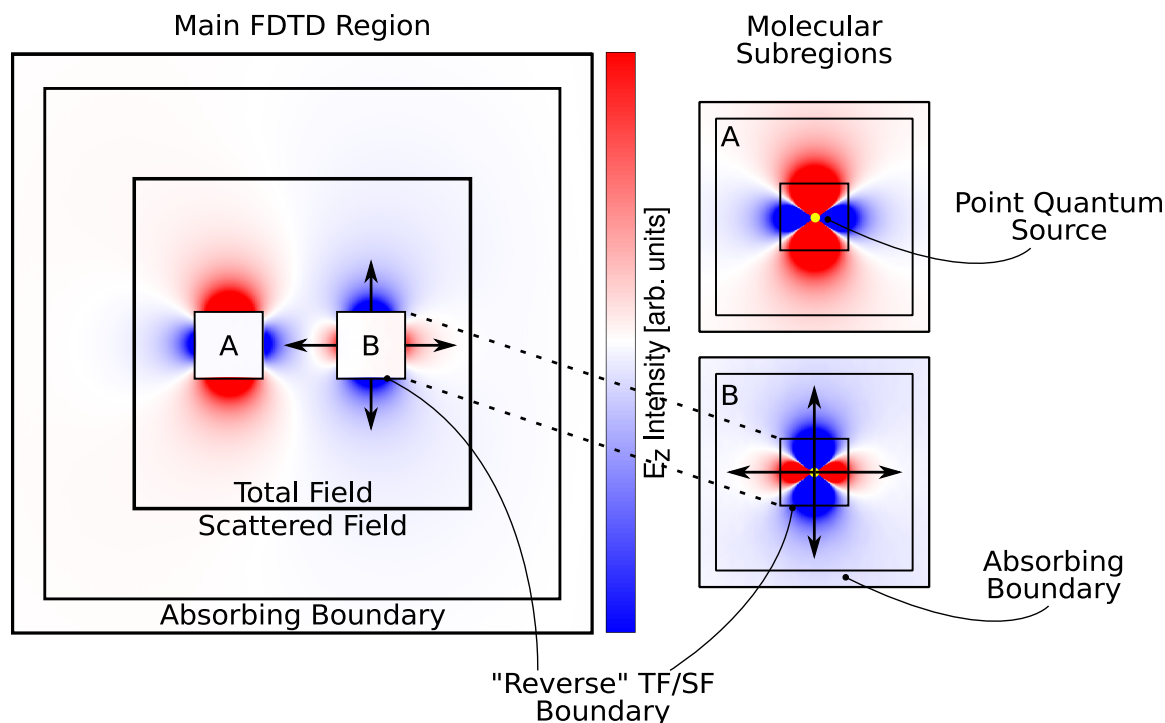


Figure 2: Schematic of the multiscale quantum/classical approach. A main finite-difference time-domain (FDTD) region contains the background and any potential metal nanostructures, while each quantum molecule is contained within its own FDTD subregion. These molecules are excited via the electric field in the main region, but emit into their own auxiliary sub-region to prevent self-excitation. These emitted fields are then introduced into the main region using reverse total-field/scattered-field (TF/SF)-like interfaces (arrows). This approach allows for an arbitrary number of quantum molecules treated using any quantum method.

interfaces act as sources for the TF region. Finally, each molecular subregion has its own absorbing boundary to prevent reflections.

This technique has three advantages: (1) It does not assume any analytic form for the molecular fields and is thus valid for any quantum point source (e.g., non-dipolar), (2) if the grid parameters are consistent between the main and molecular FDTD regions, artifacts from the interfaces will be minimal, and (3) it can be extended to a large number of molecules, as the computational cost associated with each subregion is insignificant compared to the main grid, and each region can be computed in parallel.

2.3 *N*-Level System with Dephasing

The above-described embedding technique is valid for virtually any quantum treatment of the molecules (e.g., time-dependent Schrödinger equation, time-dependent density functional theory, etc). For simplicity, here we will use a phenomenological *N*-level picture for the quantum dynamics. In the density matrix representation, the equation of motion for is governed by the von Neumann equation:

$$i\frac{\partial\rho(t)}{\partial t} = [\rho(t), H(t)] \quad (2)$$

where for a *N*-level system *H* and *ρ* are *N* × *N* matrices. To incorporate dephasing, it is convenient to instead use a Liouville representation:

$$i\frac{\partial||\rho(t)\rangle\rangle}{\partial t} = \mathcal{L}||\rho(t)\rangle\rangle, \quad (3)$$

where $||\rho(t)\rangle\rangle$ is the density vector (length N^2) and \mathcal{L} is the Liouville operator (matrix size $N^2 \times N^2$)

$$||\rho(t)\rangle\rangle = \begin{pmatrix} \rho_{11}(t) \\ \rho_{12}(t) \\ \vdots \\ \rho_{1N}(t) \\ \rho_{21}(t) \\ \vdots \\ \rho_{NN}(t) \end{pmatrix} \quad (4)$$

The Liouville operator can be constructed from the Hamiltonian by converting from 2-index to 4-index form:

$$\mathcal{L}_{jklm} = H_{jl}\delta_{km} - H_{mk}\delta_{jl} \quad j, k, l, m \in [1, N] \quad (5)$$

where, without dephasing, the Hamiltonian is given by

$$\mathbf{H}(t) = \mathbf{H}^0 - \boldsymbol{\mu} \cdot \mathbf{E}(t) \quad (6)$$

and $\boldsymbol{\mu}$ is the transition dipole (tensor) operator, $\mathbf{E}(t)$ is a time dependent electric field, and $\mathbf{H}_{kl}^0 = \varepsilon_k \delta_{kl}$. The transition dipole matrix elements in direction d are

$$\mu_{kl}^d = -\langle k|d|l\rangle, \quad (d = \{x, y, z\}) \quad (7)$$

The 4-index \mathcal{L}^0 operator ($N \times N \times N \times N$) is then reshaped to 2-index for ($N^2 \times N^2$). For example, if $N = 2$

$$\mathcal{L}^0 = \begin{pmatrix} 0 & \mu_{12} \cdot E & -\mu_{12} \cdot E & 0 \\ \mu_{12} \cdot E & -\Delta\varepsilon_{2-1} + \Delta\mu_{2-1} \cdot E & 0 & -\mu_{12} \cdot E \\ -\mu_{12} \cdot E & 0 & \Delta\varepsilon_{2-1} - \Delta\mu_{2-1} \cdot E & \mu_{12} \cdot E \\ 0 & -\mu_{12} \cdot E & \mu_{12} \cdot E & 0 \end{pmatrix} \quad (8)$$

where the energy of the transition is defined as $\Delta\varepsilon_{l-k} = \varepsilon_l - \varepsilon_k$ (e.g., $\Delta\varepsilon_{2-1} = \varepsilon_2 - \varepsilon_1$), and the difference in static dipole moments is defined as $\Delta\mu_{l-k} = \mu_l - \mu_k$. For a three level system (N=3), we get

$$\mathcal{L}^0 = \begin{pmatrix} 0 & \mu_{12} \cdot E & \mu_{13} \cdot E & -\mu_{12} \cdot E & 0 \\ \mu_{12} \cdot E & -\Delta\varepsilon_{2-1} + \Delta\mu_{2-1} \cdot E & \mu_{21} \cdot E & 0 & -\mu_{12} \cdot E \\ \mu_{13} \cdot E & \mu_{23} \cdot E & -\Delta\varepsilon_{3-1} + \Delta\mu_{3-1} \cdot E & 0 & 0 \\ -\mu_{12} \cdot E & 0 & 0 & \Delta\varepsilon_{2-1} - \Delta\mu_{2-1} \cdot E & \mu_{12} \cdot E \\ 0 & -\mu_{12} \cdot E & 0 & \mu_{12} \cdot E & 0 \\ 0 & 0 & -\mu_{12} \cdot E & \mu_{13} \cdot E & \mu_{23} \cdot E \\ -\mu_{13} \cdot E & 0 & 0 & -\mu_{23} \cdot E & 0 \\ 0 & -\mu_{13} \cdot E & 0 & 0 & -\mu_{23} \cdot E \\ 0 & 0 & -\mu_{13} \cdot E & 0 & 0 \\ 0 & 0 & -\mu_{13} \cdot E & 0 & 0 \\ 0 & 0 & 0 & -\mu_{13} \cdot E & 0 \\ -\mu_{12} \cdot E & 0 & 0 & 0 & -\mu_{13} \cdot E \\ \mu_{13} \cdot E & -\mu_{23} \cdot E & 0 & 0 & 0 \\ \mu_{23} \cdot E & 0 & -\mu_{12} \cdot E & 0 & 0 \\ -\Delta\varepsilon_{3-2} + \Delta\mu_{3-2} \cdot E & 0 & 0 & 0 & -\mu_{23} \cdot E \\ 0 & \Delta\varepsilon_{3-1} - \Delta\mu_{3-1} \cdot E & \mu_{12} \cdot E & \mu_{13} \cdot E \\ 0 & -\mu_{12} \cdot E & \Delta\varepsilon_{3-2} - \Delta\mu_{3-2} \cdot E & \mu_{23} \cdot E \\ -\mu_{23} \cdot E & \mu_{13} \cdot E & \mu_{23} \cdot E & 0 \end{pmatrix} \quad (9)$$

Now if we want to introduce dephasing of the coherences (i.e., T_2 lifetimes) in a Redfield-like picture,⁴⁹ we add an imaginary part to the Liouville operator

$$\mathcal{L} = \mathcal{L}^0 + i\mathcal{L}^d \quad (10)$$

In 4-index form:

$$\mathcal{L}_{j,k,l,m}^d = \gamma_{jk} \delta_{jk,jk}, \quad j \neq k \quad (11)$$

where $\gamma_{jk} = \gamma_{kj}$ and the dephasing parameters are the inverse of the T_2 lifetimes:

$$T_{2,jk} = \frac{1}{\gamma_{j,k}} \quad (12)$$

Note that we have not included T_1 lifetimes here (energy loss/damping) although this is easily done. E.g. for $N = 2$

$$\gamma_{12} = \gamma_{21} = -\frac{i}{T_{2,12}} \quad (13)$$

and zero for other terms. In 2-index form:

$$\mathcal{L}^d = \begin{pmatrix} 0 & 0 & 0 & 0 \\ 0 & -i\gamma_{12} & 0 & 0 \\ 0 & 0 & -i\gamma_{12} & 0 \\ 0 & 0 & 0 & 0 \end{pmatrix} \quad (14)$$

For a three level system, the 4-index dephasing Liouvillian is:

$$\mathcal{L}_{12,12}^d = \mathcal{L}_{21,21}^d = -i\gamma_{12} \quad (15a)$$

$$\mathcal{L}_{13,13}^d = \mathcal{L}_{31,31}^d = -i\gamma_{13} \quad (15b)$$

$$\mathcal{L}_{23,23}^d = \mathcal{L}_{32,32}^d = -i\gamma_{23} \quad (15c)$$

(other terms are zero). In the 2-index form:

$$\mathcal{L}^d = \begin{pmatrix} 0 & 0 & 0 & 0 & 0 & 0 & 0 & 0 & 0 \\ 0 & -i\gamma_{12} & 0 & 0 & 0 & 0 & 0 & 0 & 0 \\ 0 & 0 & -i\gamma_{13} & 0 & 0 & 0 & 0 & 0 & 0 \\ 0 & 0 & 0 & -i\gamma_{12} & 0 & 0 & 0 & 0 & 0 \\ 0 & 0 & 0 & 0 & 0 & 0 & 0 & 0 & 0 \\ 0 & 0 & 0 & 0 & 0 & -i\gamma_{23} & 0 & 0 & 0 \\ 0 & 0 & 0 & 0 & 0 & 0 & -i\gamma_{13} & 0 & 0 \\ 0 & 0 & 0 & 0 & 0 & 0 & 0 & -i\gamma_{23} & 0 \\ 0 & 0 & 0 & 0 & 0 & 0 & 0 & 0 & 0 \end{pmatrix} \quad (16)$$

Now, if we assume the system starts purely in the ground state

$$||\rho(0)\rangle\rangle = \begin{pmatrix} 1 \\ 0 \\ \vdots \\ 0 \end{pmatrix} \quad (17)$$

we can propagate $||\rho(t)\rangle\rangle$ by integrating the equation of motion:

$$||\rho(t + \Delta t)\rangle\rangle = \hat{U} ||\rho(t)\rangle\rangle \quad (18)$$

where the propagator $\hat{U} \equiv e^{-i\mathcal{L}(t)\Delta t}$. In simple cases, the matrix exponentiation can be done using diagonalization, but other methods, such as power series expansion, can be used.^{50,51}

Now, the expectation value of the polarization can be computed from the density vector:

$$\langle p^d(t) \rangle = p^d(t) = \langle \mu^d | \rho(t) \rangle \quad (19)$$

where μ^d is the dipole superoperator in the d -direction:

$$\mu^d = \begin{pmatrix} \mu_{11}^d \\ \mu_{12}^d \\ \mu_{13}^d \\ \vdots \\ \mu_{1N}^d \\ \vdots \\ \mu_{NN}^d \end{pmatrix} \quad (20)$$

Note, this includes on-diagonals μ_{kk} which represent static dipole moments of the ground and excited states. The time derivative of the polarization (Eq. 19) is required for coupling to the FDTD:

$$\frac{\langle p(t) \rangle}{dt} = \frac{d}{dt} \langle \langle \mu | \rho(t) \rangle \rangle \quad (21a)$$

$$\frac{d}{dt} \langle p(t) \rangle = \langle \langle \mu | \frac{d\rho(t)}{dt} \rangle \rangle \quad (21b)$$

Since

$$\frac{d\rho(t)}{dt} = -i\mathcal{L}\rho(t) \quad (22)$$

Eq. 21a becomes

$$\frac{dp}{dt} = -i \langle \langle \mu | \mathcal{L}\rho \rangle \rangle \quad (23)$$

This single molecule (microscopic) polarization is scaled by the volume of a simulation voxel ($\Delta V = \Delta x \times \Delta y \times \Delta z$) to obtain the macroscopic polarization:

$$\frac{dP}{dt} = \frac{dp}{dt} \Delta V = J(t) \quad (24)$$

This becomes a current source term in Maxwell's equations via Eq. 1a.

3 Results

3.1 Validation of FDTD

Before discussing the coupled plasmon/molecule case, we validate the electrodynamics and FDTD/QM approaches separately. For the electrodynamics, we developed our own FDTD code to allow for ease of integration with the quantum code. For each simulation, the total volume was approximately $2281 \times 2281 \times 2281 \text{ nm}^3$. Convergence with grid spacing was testing for $\Delta x = \Delta y = \Delta z = 16, 12, 8 \text{ au} = 8.47, 6.35, 4.23 \text{ \AA}$. For the finest grid, this corresponds to 539^3 total grid points. The time step was taken to be 0.8 times the Courant stability limit which corresponds to $0.036 \text{ a.u.} = 8.71 \times 10^{-4} \text{ fs}$. Each simulation was allowed to continue until the fields decayed to 0.1% of the maximum intensity, corresponding to about 3500 au of time. This required roughly 9.72×10^4 time steps, which took about 20 hours on 16 processors (OpenMP parallelized) and used approximately 160 GB of RAM.

For each simulation, the system was initialized using the TF/SF boundary with an x -directed, z -polarized broadband plane-wave excitation centered on the plasmon frequency. The pulse was chosen to be a discrete Ricker Wavelet to minimize grid artifacts:

$$f_r[q] = \left(1 - 2\pi^2 \left[\frac{S_c q}{N_p} - M_d\right]^2\right) \exp\left(-\pi^2 \left[\frac{S_c q}{N_p} - M_d\right]^2\right) \quad (25)$$

where S_c is the Courant stability number (i.e., 0.8), N_p is the number of points per wavelength at the center frequency ω_0 and is defined by

$$N_p = \frac{S_c}{\omega_0 \Delta t} \quad (26)$$

and the temporal delay M_d is the delay multiple. This pulse contains no DC component, and its spectral content is set by a single parameter (i.e., ω_0).⁵²

After excitation, the energy flow into and out of the system is measured as a function of time via a scattering flux monitor located outside the total field region (in the scattering

region) and an absorption flux monitor located inside the total field region. By collecting the outgoing electric and magnetic fields on these flux monitors, we can obtain extinction properties of the system (molecule, nanoparticle, combined, etc). See Supporting Information for details.

Before progressing to the coupled quantum/FDTD case, we first validate our FDTD implementation for a single gold nanoparticle. As is commonly done, the frequency-dependent permittivity of the metal is modeled as a sum of Lorentzians

$$\varepsilon(\omega) = \varepsilon_{\infty} + \varepsilon_0 + \sum_{j=1}^{N_L} \frac{\beta_j}{\omega_j^2 - i\alpha_j\omega - \omega^2} \quad (27)$$

where α_j , ω_j , and β_j are real material-dependent parameters. These parameters can be directly incorporated through the auxiliary difference equation technique.⁵³ For the parameters, we use the $N_L = 9$ Lorentzian fit to experimental bulk values obtained by Neuhauser et al.⁵⁴ This fit is valid over the energy range between 0.6 – 6.7 eV.

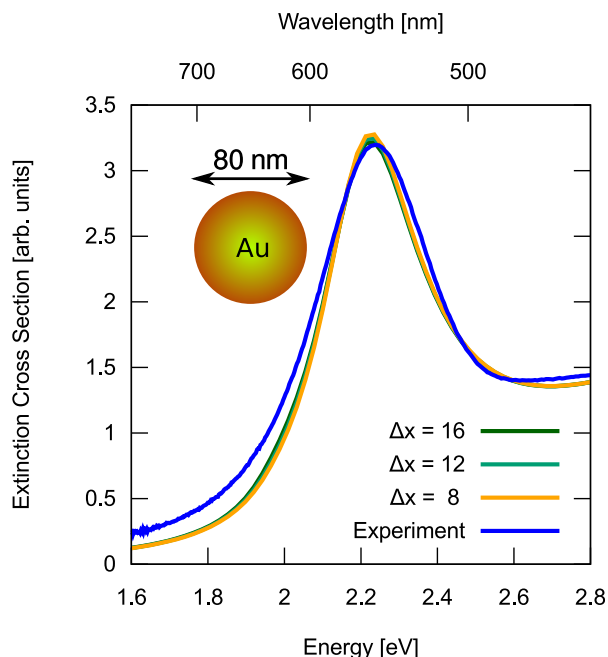


Figure 3: Comparison of FDTD computed and experimentally measured extinction (absorption + scattering) for a 80 nm diameter gold nanoparticle. The computed spectra are insensitive to grid and are consistent with experiment.

For this validation we computed the extinction (absorption + scattering) of a single 80 nm diameter gold nanosphere in water ($\epsilon_r = 1.335$) with various grid spacings and compared it to the experimental extinction measured with a UV/Vis spectrophotometer. Fig. 3 shows the spectra for various grid spacings. Overall the spectrum is relatively insensitive to grid, and agrees well with experiment in the region of the plasmon resonance. Deviations at lower (~ 1.8 eV) and higher (~ 2.5 eV) are likely due to polydispersity in the experiment. Based on these results, we henceforth use a grid spacing of $\Delta x = 8$ au = 4.23 Å for subsequent calculations of this size nanoparticles.

3.2 Energy coupling between two molecules

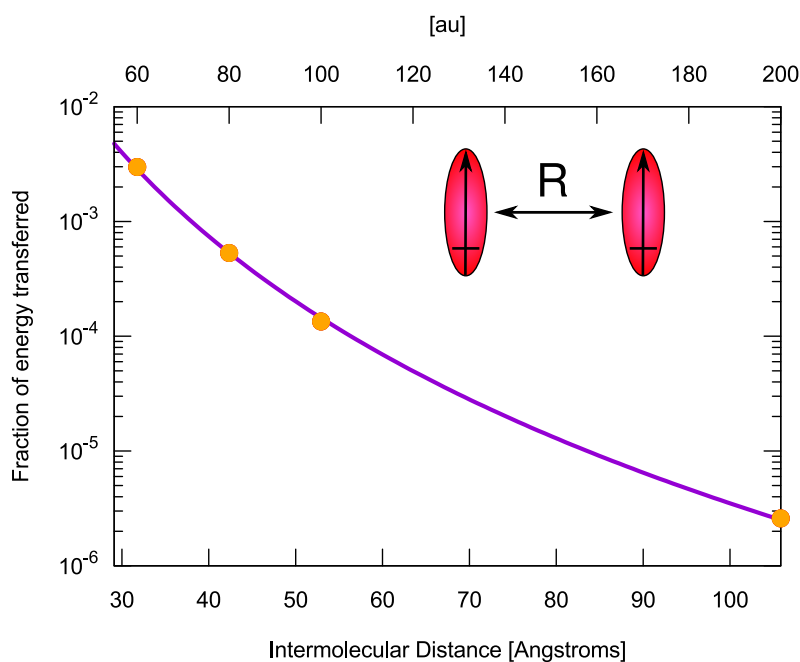


Figure 4: Computed resonant energy transfer between a pair of two-level chromophores as a function of separation (R). The transition dipole moments are shown with arrows. The fractional energy transfer from an excited (donor) molecule to the acceptor follows a $1/R^6$ trend, consistent with a Förster-like process (dipole-dipole coupling).

To validate our multi-molecule embedding scheme, we computed resonant energy transfer between a pair of spatially separated two-level molecules with aligned transition dipole moments. Here, to emphasize the effect, we chose each to have a non-physical transition dipole

moment of 57 au = 144 D. The frequency was chosen to be 0.073 au = 2.0 eV. For this simulation, the subregion around each molecule was 30 au wide with an absorbing boundary beyond each TF-MF boundary. The left molecule was initialized via a delta kick excitation. The transfer was quantified by computing the maximum energy on the right molecule as a fraction of the maximum energy on the left molecule. Figure 4 shows this fractional energy transfer as a function of intermolecular separation R . The observed $1/R^6$ behavior is characteristic of a Förster-like resonance energy transfer (FRET) mechanism, which arises from long-range dipole-dipole interactions.^{55–57} These interactions are mediated by the classical electrodynamics background. This type of interaction can be challenging for purely quantum approaches such as TDDFT, which can have an incorrect asymptotic potential and/or basis set limitations. Thus, beyond the context of plasmon/molecule systems, this approach may also be suitable for capturing long-range energy transfer using TDDFT.

3.3 Plasmon/Molecule Coupling

Now we turn to the main topic of this paper, namely computing the coupled excitations of plasmons with multiple nearby chromophores. Here we study the system consisting of a 80 nm gold NP with a full monolayer of malachite green molecules adsorbed on the surface (See Fig. 1). Previous experimental studies on this system have exhibited strong coupling between the plasmons and excitations on the dyes, which can be observed via a difference UV-visible extinction spectrum.³⁴ These systems have well-characterized nanoparticle sizes (via transmission electron microscopy) and known surface coverage (via second harmonic generation isotherms). Questions remain, however, about the physical origins of the observed features in the coupling spectra, as well as the orientation (transition dipole angle) and distance of the dyes molecules from the NP surface. In this section, we present simulations for interpreting these difference spectra and approximating the geometries of the dyes with respect to the NP.

3.3.1 Parametrizing Monolayer of Quantum Molecules

We model malachite green as a three-level molecule, focusing only on the transitions at 2.02 eV and 2.13 eV. The molecular parameters were determined by fitting the experimental spectrum to the sum of two Lorentzian functions, with the peak positions yielding $\Delta\epsilon_{2-1} = 0.07423$ au = 2.020 eV and $\Delta\epsilon_{3-1} = 0.07822$ au = 2.129 eV, respectively. The oscillator strengths were found by integrating the extinction, which in turn gives the transition dipole moments ($\mu_{12} = 1.985$ au = 5.046 D and $\mu_{13} = 1.575$ au = 4.003 D). For the lifetimes, it is generally impossible to deconvolute an experimental absorption peak into T_1 (damping) and T_2 (dephasing) contributions. For simplicity we assume only dephasing, with the corresponding lifetimes fit to the full width half maximum of the experiment. Here, $T_{12} = 481.4$ au = 11.65 fs and $T_{13} = 291.9$ au = 7.061 fs, corresponding to the dephasing times between states $|1\rangle$ and $|2\rangle$ and $|1\rangle$ and $|3\rangle$, respectively.

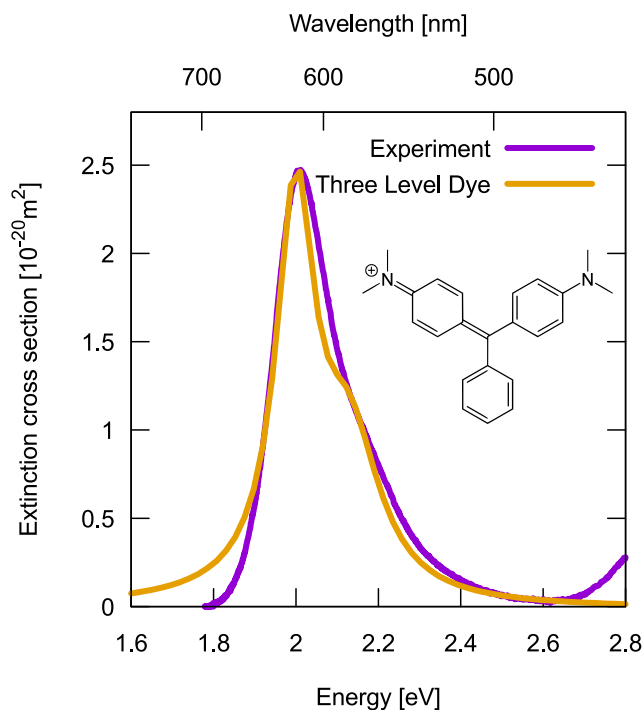


Figure 5: Computed extinction spectra for a single malachite green molecule, modeled as a three-level system with parameters fit to match experiment.

Experimentally, we previously determined that each 80 nm Au NP had $M \approx 9200$

1
2
3 molecules adsorbed to the surface.³⁴ Although the formalism could be applied to directly
4
5 model this system, for simplicity we instead model the monolayer as two “super” molecules
6
7 with scaled-up transition dipole moments. This allows us to mimic the response of malachite
8
9 green covering the entire gold surface using only two quantum molecules. A super molecule
10
11 approach implicitly assumes a particular orientation of each molecule with respect to the
12
13 surface and neglects coupling between molecules.
14

15 We determined the super molecule transition dipole moments such that the absorp-
16
17 tion of the pair matches the expected response of a fully covered nanoparticle. Neglecting
18
19 molecule/molecule coupling, the scaling factor can be approximated from the experimentally
20
21 measured surface coverage M . Since absorption scales linearly with the number of molecules,
22
23 the total absorption of a collection of independent oscillators is given by:
24

$$25 \quad \tilde{\sigma} = \widetilde{M}\sigma \quad (28)$$

26
27 where σ is the absorption of a single molecule, $\tilde{\sigma}$ is the absorption of the collection of
28
29 molecules, and \widetilde{M} is an effective number of molecules. For an isotropic arrangement, \widetilde{M} is
30
31 simply the number of molecules in solution. For the case of molecules adsorbed to a spherical
32
33 nanoparticle with a well-defined angle with respect to the normal, and for a particular light
34
35 polarization (say z), this becomes an orientational average. This is a surface integral of the
36
37 transition dipoles dotted into the normal, which accounts for alignment of the molecules
38
39 with respect to the z -polarized light field:
40
41
42
43
44

$$45 \quad \widetilde{M} = M \int_0^\pi d\theta \sqrt{\frac{\langle \cos^2(\theta) \rangle}{\langle \cos^2(0) \rangle}} = M \frac{1}{\sqrt{2}} \quad (29)$$

46
47 Now, since absorption is directly proportional to the square of the transition dipole,
48
49 $\tilde{\sigma} \propto \tilde{\mu}^2$, the effective “super” transition dipole moment is given by:
50
51

$$52 \quad \tilde{\mu} = \sqrt{\widetilde{M}}\mu \quad (30)$$

A single molecule is unable to capture molecule-plasmon-molecule polariton modes so we instead used two super dyes positioned at the $\theta = 0$ and $\theta = 180^\circ$ poles of the nanoparticle. Before proceeding to the nanoparticle case, we first validated the super molecule approach by comparing the z -polarized extinction of two dyes with purely z -oriented dipole moments against that of four dyes, each located at some angle θ with respect to the z -axis. For a pair, the transition dipole is scaled by an additional $\frac{1}{\sqrt{2}}$ such that the absorption cross section is the same (see Eq. 30). Fig. 6 shows the calculated extinction spectra for these two systems. Note here, for molecules the scattering is negligible so the extinction is predominantly absorption. The two are essentially identical, demonstrating that two super molecules can represent an arbitrary number of molecules, at least in the limit of no molecular coupling.

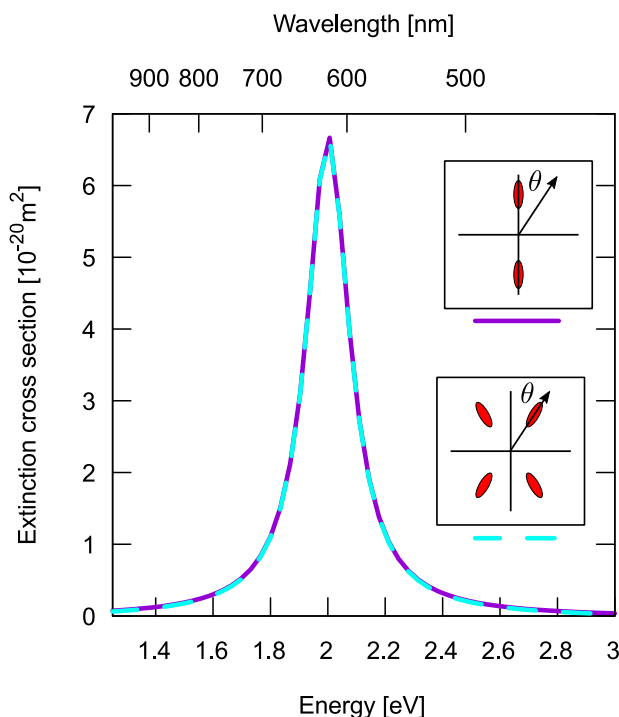


Figure 6: Computed z -polarized extinction of four molecules ($\theta = 30^\circ, 150^\circ, 210^\circ,$ and 330°) is captured correctly by two “super” molecules ($\theta = 0^\circ, 180^\circ$). Here, the long axis of the red ovals point along the direction of the transition dipole. This can be extended to modeling an arbitrary number of molecules using only two oscillators, at least in the limit of negligible molecule-molecule interactions.

3.3.2 Au Nanoparticle/Malachite Green Difference Spectra

Using this approach we now model the coupled plasmon-molecule polariton response of Au NP with malachite green adsorbed on the surface. This is a follow up on our previous experimental results.³⁴ For these coupled nanoparticle/molecule simulations, we parameterized our grid using the best grid spacing from the convergence test of gold in Fig. 3 (i.e., $\Delta x = 8$ au). The malachite green monolayer was modeled using a pair of three-level super molecules, with the molecular parameters fit to experiment (See Sec. 3.3.1). For the surface coverage, we use our experimentally determined value of $M \approx 9200$, which was obtained using second harmonic generation (SHG) isotherm for a 80 nm gold nanoparticle.³⁴

The physical distance between the NP surface and dye monolayer (ℓ), as well as the angle of the transition dipole with respect to the normal (η) both remain unknown. As first approximation, we estimated the distance by measuring the length of mercaptosuccinic acid (MSA), the capping agent molecule, which is chemically bound to the surface of gold, and the length from the edge of the dye to its center. Additionally, since these dyes are held at the surface via electrostatic interactions, we estimate that there are at least 1-2 water shells between the dye and MSA. For the angle, previous studies attribute observed results to a tilt angle of the dyes, but the angle remains unclear. Moreover, the molecular tilt angle is potentially different from the transition dipole angle. Thus for this paper, we compute the plasmon-molecule spectra for a range of separations (ℓ) and transition dipole angles (η) to determine rough values.

First, we explore the effect of transition dipole angle on the coupling. To start, we pick the monolayer distance to be $\ell = 48$ au = 25.4 Å. This is consistent with approximately 1-2 shells of water between the surface and the center of the dye. Figure 7 shows resulting z -polarized coupling spectra for a range of transition dipole angles. As in experiment, this extinction spectrum was obtained by computing the spectrum of the NP+molecule system, then subtracting the extinction spectrum of the lone gold nanoparticle, as well as that of a solution of M molecules. For the molecule subtraction, to be consistent with experiment

we used a ensemble average of molecular orientations, which corresponds to $\frac{1}{3}M$ for the z -polarization.

Figure 7 shows the difference in extinction as a result of the molecule-plasmon interactions, that is, in the absence of plasmon/molecule coupling, the difference extinction would be zero. In this case, the residuals reveal a Fano-like resonance centered at the molecular frequency $\Delta\varepsilon_{2-1}$, which results in two additional peaks. The lower energy peak corresponds to an in-phase coupled polaritonic mode $|P-\rangle$ involving the primary dye absorption ($|1\rangle \rightarrow |2\rangle$ transition) and the plasmon. This mode is significantly red-shifted from the uncoupled molecular mode. The complimentary out-of-phase polariton $|P+\rangle$ is blue-shifted and lower in magnitude. Additionally, there is a prominent negative feature at ~ 2.02 eV which corresponds to depletion of the main molecular mode at $\omega_m = \Delta\varepsilon_{2-1}$, i.e., energy transferred from the molecule to the plasmon, forming the polaritonic states $|P-\rangle$ and $|P+\rangle$. The corresponding plasmon depletion and second molecular mode (i.e., $\Delta\varepsilon_{3-1}$) overlap the $|P+\rangle$ polariton and are not clearly visible due to the small μ_{13} transition dipole for this molecular mode. These signals would likely be more prominent for the case of a smaller nanoparticle, where the cross section of the molecules would be closer in magnitude to that of the plasmon.

The effect of transition dipole angle η on these polaritonic states is also shown in Figure 7. Regardless of angle, the frequency of the $|P+\rangle$ polariton is ~ 2.14 eV, while the magnitude decreases with increasing η . In contrast, the $|P-\rangle$ frequency blue-shifts and the magnitude decreases with increasing η . At a distance of $\ell = 25.4$ Å, for example, a transition dipole angle of $\eta = 60^\circ$ gives the best agreement with experiment, for both the frequency (~ 1.89 eV) of the modes as well as the relative magnitudes. The energy difference between the two polariton peaks, ΔE_P , corresponds to the splitting energy. This is a measure of the coupling strength between the molecular and plasmon excitations. Our model predicts an approximate splitting energy of $\Delta E_P = 263$ meV for malachite green and a 80 nm Au NP. This is in agreement with our experimental difference extinction measurements (Fig. 7C).³⁴

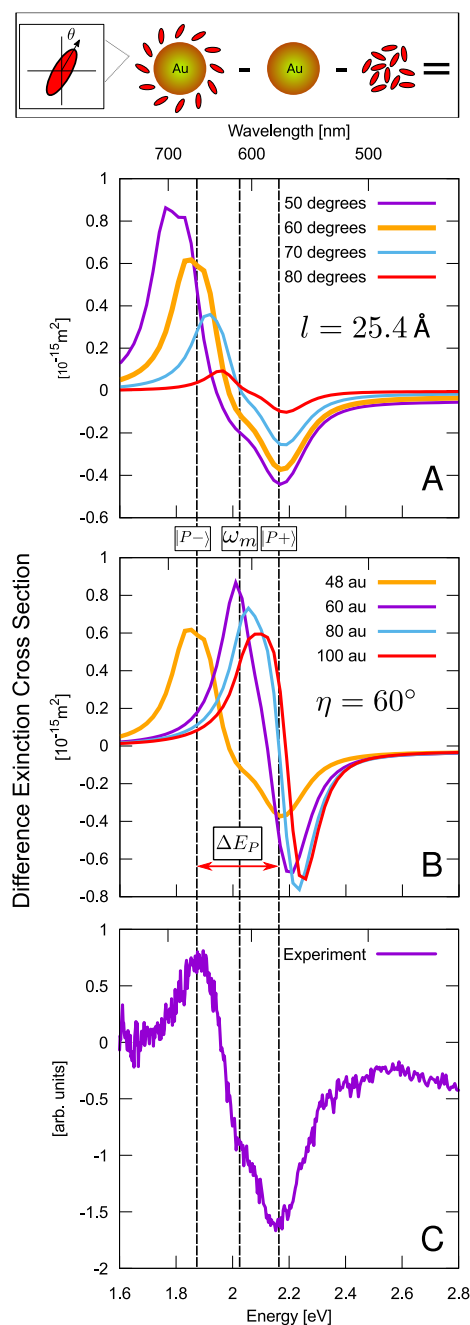


Figure 7: Comparison of FDTD computed and experimentally measured difference extinction spectra (coupled system – pure Au NP – dye solution) for a 80 nm diameter Au nanoparticle (NP) surrounded by malachite green molecules. The difference spectra reveals the coupling between the plasmon and molecular excitations. The system is modeled using two “super” dye molecules by fixing either the separation distance from the NP surface (Panel A) or transition dipole angle (Panel B) and varying the other (e.g., Panel A $l = 25.4 \text{ \AA}$ and vary η). The residual Fano-type resonances correspond to an in-phase polariton $|P- \rangle$ (lower energy) and an out-of-phase polariton $|P+ \rangle$ (higher energy). The depletion in the brightest molecular mode is visible at 2.02 eV (ω_m). The corresponding plasmon depletion and second molecular mode overlap the $|P+ \rangle$ polariton and are not clearly visible.³⁴

1
2
3
4
5
6
7
8
9
10
11
12
13
14
15
16
17
18
19
20
21
22
23
24
25
26
27
28
29
30
31
32
33
34
35
36
37
38
39
40
41
42
43
44
45
46
47
48
49
50
51
52
53
54
55
56
57
58
59
60

Additionally, since the exact distance ℓ between the metal surface and the malachite green monolayer is not implicitly known, we also explored its effect on the splitting energy ΔE_P . Figure 7B shows the difference spectra with a fixed transition dipole angle ($\theta = 60^\circ$) and various monolayer distances ($\ell = 48, 60, 80, 100$ au). The splitting energy decreases with increasing ℓ , as evidenced by a blue-shifting $|P-\rangle$ (in-phase) polariton frequency. The magnitude, on the other hand, is relatively insensitive to ℓ . This is likely due to the relatively large separation from the surface, where the exponentially decaying electric field has a shallow gradient. The $|P+\rangle$ (out-of-phase) polariton frequency and magnitude appears relatively insensitive with increasing ℓ . From these results, however, it is clear that the splitting energy ΔE_P decreases with ℓ .

Since both η and ℓ affect the splitting energy, there is some ambiguity in using these simulations to determine the molecular geometry. Without some experimental measure of either of the parameters, it is difficult to conclusively approximate their values. In principle, a full 2D parameter scan might be illustrative, but choosing a “best” angle and distance by matching ΔE_P might still be ambiguous. Regardless, assuming $\ell = 25.4$ Å gives a transition dipole angle of $\eta = 60^\circ$ which is consistent with a tilted malachite green molecule. Future molecular simulation studies will give more insight into the geometry of malachite green adsorbed to the surface of Au NP.

4 Conclusions

In conclusion, we have presented a multiscale method for computing the coupled plasmon/molecule excitations for systems containing an arbitrary number of molecules on the surface of a metal. This uses finite-difference time-domain (FDTD) for the classical fields and quantum mechanical for the electron dynamics on each molecule. In this paper, we derive the expression for an N -level Hamiltonian with dephasing via a Redfield-like treatment, but this approach can also be extended to use any time-dependent quantum method.

We validated our results for the simple cases of a lone gold nanoparticle, as well as resonant energy transfer between two isolated molecules. The technique was then extended to model the extinction spectra of gold nanoparticles with an adsorbed monolayer of malachite green described using two “super molecules.” This was used to predict the orientation of the dye molecules (or at least that of their transition dipole), as well as the separation of the monolayer from the gold surface. Our results capture the experimentally observed polariton modes (coupled plasmon/molecule excitations) and agree with the observed experimental splitting energy of ~ 263 eV, with a “best guess” for the distance of $\ell \sim 25.4$ Å, and a transition dipole angle of $\eta \sim 60^\circ$.

Both quantities ℓ and η are difficult to measure experimentally, but are crucial for interpreting spectra and for applications spanning molecular sensing, plasmonic photovoltaics, and near-field photocatalysis. As the coupling depends simultaneously on both transition dipole angle of the molecule, as well as the separation from the surface, it is difficult to conclusively assign their values from these simulations. Nevertheless, this ambiguity can be remedied if one parameter is known, either from experimental measurements, or computed using molecular simulations. In subsequent studies, to include potential molecule/molecule interactions, we will use a larger number of oscillators rather than two “super molecules”. The agreement of these results, however, with experiment indicates there is little interaction between dye molecules on the surface, and the majority of the coupling is due to interaction between the molecule and plasmon.

Finally, this method can be extended beyond the simple N -level model using real-time quantum chemistry techniques such as time dependent Hartree-Fock,^{58–60} time-dependent density functional theory,^{51,61–64} configuration interaction,^{65,66} coupled cluster,^{67,68} and two-electron reduced density matrix methods.⁶⁹ Moreover, to mitigate the computational cost of multiple molecules, the FDTD as well as each molecule can be computed in parallel, either using traditional MPI-like parallelization, or by using accelerator cards. Finally, spectral acceleration techniques such as filter diagonalization^{70,71} or Padé approximants,⁷² can

significantly decrease simulations times.

Acknowledgement

This research was supported by the Louisiana Board of Regents Research Competitiveness Subprogram under contract number LEQSF(2014-17)-RD-A-03. This material is based upon work supported by the National Science Foundation under the NSF EPSCoR Cooperative Agreement No. EPS-1003897. Support from the 2015 Ralph E. Powe Junior Faculty Enhancement Award from Oak Ridge Associated Universities is gratefully acknowledged. We would like to thank Rami Khoury for valuable discussions. Contributions by Jelaine Cunnanan are also acknowledged, who was supported by National Science Foundation REU award #ACI-1560410.

Supporting Information Available

Detailed procedures on setting up flux monitors to calculate absorption and scattering cross sections from FDTD. This material is available free of charge via the Internet at <http://pubs.acs.org/>.

References

- (1) El-Sayed, I. H.; Huang, X.; El-Sayed, M. A. Surface plasmon resonance scattering and absorption of anti-EGFR antibody conjugated gold nanoparticles in cancer diagnostics: applications in oral cancer. *Nano Lett.* **2005**, *5*, 829–834.
- (2) El-Sayed, I. H.; Huang, X.; El-Sayed, M. A. Selective laser photo-thermal therapy of epithelial carcinoma using anti-EGFR antibody conjugated gold nanoparticles. *Cancer Lett.* **2006**, *239*, 129–135.
- (3) Kamat, P. V. Photophysical, photochemical and photocatalytic aspects of metal nanoparticles. *J. Phys. Chem. B* **2002**, *106*, 7729–7744.

- (4) Narayanan, R.; El-Sayed, M. A. Catalysis with transition metal nanoparticles in colloidal solution: nanoparticle shape dependence and stability. *J. Phys. Chem. B* **2005**, *109*, 12663–12676.
- (5) Haes, A. J.; Van Duyne, R. P. A nanoscale optical biosensor: sensitivity and selectivity of an approach based on the localized surface plasmon resonance spectroscopy of triangular silver nanoparticles. *J. Am. Chem. Soc.* **2002**, *124*, 10596–10604.
- (6) Sperling, R. A.; Gil, P. R.; Zhang, F.; Zanella, M.; Parak, W. J. Biological applications of gold nanoparticles. *Chem. Soc. Rev.* **2008**, *37*, 1896–1908.
- (7) Freddi, S.; D'Alfonso, L.; Collini, M.; Caccia, M.; Sironi, L.; Tallarida, G.; Caprioli, S.; Chirico, G. Excited-State Lifetime Assay for Protein Detection on Gold Colloids- Fluorophore Complexes. *J. Phys. Chem. C* **2009**, *113*, 2722–2730.
- (8) Prigodich, A. E.; Lee, O.-S.; Daniel, W. L.; Seferos, D. S.; Schatz, G. C.; Mirkin, C. A. Tailoring DNA structure to increase target hybridization kinetics on surfaces. *J. Am. Chem. Soc.* **2010**, *132*, 10638–10641.
- (9) Kamat, P. V. Meeting the clean energy demand: nanostructure architectures for solar energy conversion. *J. Phys. Chem. C* **2007**, *111*, 2834–2860.
- (10) Bardhan, R.; Grady, N. K.; Cole, J. R.; Joshi, A.; Halas, N. J. Fluorescence enhancement by Au nanostructures: nanoshells and nanorods. *ACS Nano* **2009**, *3*, 744–752.
- (11) Brown, S. D.; Nativo, P.; Smith, J.-A.; Stirling, D.; Edwards, P. R.; Venugopal, B.; Flint, D. J.; Plumb, J. A.; Graham, D.; Wheate, N. J. Gold nanoparticles for the improved anticancer drug delivery of the active component of oxaliplatin. *J. Am. Chem. Soc.* **2010**, *132*, 4678–4684.
- (12) Link, S.; El-Sayed, M. A. Shape and size dependence of radiative, non-radiative and photothermal properties of gold nanocrystals. *Int. Rev. Phys. Chem.* **2000**, *19*, 409–453.

- (13) Daniel, M.-C.; Astruc, D. Gold nanoparticles: assembly, supramolecular chemistry, quantum-size-related properties, and applications toward biology, catalysis, and nanotechnology. *Chem. Rev.* **2004**, *104*, 293–346.
- (14) Chandra, M.; Dowgiallo, A.-M.; Knappenberger Jr, K. L. Controlled plasmon resonance properties of hollow gold nanosphere aggregates. *J. Am. Chem. Soc.* **2010**, *132*, 15782–15789.
- (15) Foley IV, J. J.; McMahon, J. M.; Schatz, G. C.; Harutyunyan, H.; Wiederrecht, G. P.; Gray, S. K. Inhomogeneous Surface Plasmon Polaritons. *ACS Photon.* **2014**, *1*, 739–745.
- (16) Eck, W.; Craig, G.; Sigdel, A.; Ritter, G.; Old, L. J.; Tang, L.; Brennan, M. F.; Allen, P. J.; Mason, M. D. PEGylated gold nanoparticles conjugated to monoclonal F19 antibodies as targeted labeling agents for human pancreatic carcinoma tissue. *ACS Nano* **2008**, *2*, 2263–2272.
- (17) Maxwell, D. J.; Taylor, J. R.; Nie, S. Self-assembled nanoparticle probes for recognition and detection of biomolecules. *J. Am. Chem. Soc.* **2002**, *124*, 9606–9612.
- (18) Song, J.; Zhou, J.; Duan, H. Self-assembled plasmonic vesicles of SERS-encoded amphiphilic gold nanoparticles for cancer cell targeting and traceable intracellular drug delivery. *J. Am. Chem. Soc.* **2012**, *134*, 13458–13469.
- (19) Huang, X.; El-Sayed, I. H.; Qian, W.; El-Sayed, M. A. Cancer cell imaging and photothermal therapy in the near-infrared region by using gold nanorods. *J. Am. Chem. Soc.* **2006**, *128*, 2115–2120.
- (20) Qian, X.; Peng, X.-H.; Ansari, D. O.; Yin-Goen, Q.; Chen, G. Z.; Shin, D. M.; Yang, L.; Young, A. N.; Wang, M. D.; Nie, S. In vivo tumor targeting and spectroscopic detection with surface-enhanced Raman nanoparticle tags. *Nat. Biotechnol.* **2008**, *26*, 83–90.

- (21) Bardhan, R.; Lal, S.; Joshi, A.; Halas, N. J. Theranostic nanoshells: from probe design to imaging and treatment of cancer. *Accounts Chem. Res.* **2011**, *44*, 936–946.
- (22) Baldelli, S.; Eppler, A. S.; Anderson, E.; Shen, Y.-R.; Somorjai, G. A. Surface enhanced sum frequency generation of carbon monoxide adsorbed on platinum nanoparticle arrays. *J. Chem. Phys.* **2000**, *113*, 5432–5438.
- (23) Bordenyuk, A. N.; Weeraman, C.; Yatawara, A.; Jayathilake, H. D.; Stiopkin, I.; Liu, Y.; Benderskii, A. V. Vibrational sum frequency generation spectroscopy of dodecanethiol on metal nanoparticles. *J. Phys. Chem. C* **2007**, *111*, 8925–8933.
- (24) Vance, F. W.; Lemon, B. I.; Hupp, J. T. Enormous hyper-Rayleigh scattering from nanocrystalline gold particle suspensions. *J. Phys. Chem. B* **1998**, *102*, 10091–10093.
- (25) Butet, J.; Bachelier, G.; Russier-Antoine, I.; Jonin, C.; Benichou, E.; Brevet, P.-F. Interference between selected dipoles and octupoles in the optical second-harmonic generation from spherical gold nanoparticles. *Phys. Rev. Lett.* **2010**, *105*, 077401.
- (26) Hao, E.; Schatz, G. C.; Johnson, R.; Hupp, J. T. Hyper-Rayleigh scattering from silver nanoparticles. *J. Chem. Phys.* **2002**, *117*, 5963–5966.
- (27) Duboisset, J.; Russier-Antoine, I.; Benichou, E.; Bachelier, G.; Jonin, C.; Brevet, P. Single metallic nanoparticle sensitivity with Hyper Rayleigh Scattering. *J. Phys. Chem. C* **2009**, *113*, 13477–13481.
- (28) Chandra, M.; Knappenberger, K. L. Nanoparticle surface electromagnetic fields studied by single-particle nonlinear optical spectroscopy. *Phys. Chem. Chem. Phys.* **2013**, *15*, 4177–4182.
- (29) Dadap, J. I.; Shan, J.; Eisenthal, K. B.; Heinz, T. F. Second-harmonic Rayleigh scattering from a sphere of centrosymmetric material. *Phys. Rev. Lett.* **1999**, *83*, 4045.

- (30) Lopata, K.; Neuhauser, D. Nonlinear nanopolaritonics: Finite-difference time-domain Maxwell–Schrödinger simulation of molecule-assisted plasmon transfer. *J. Chem. Phys.* **2009**, *131*, 014701.
- (31) Arntsen, C.; Lopata, K.; Wall, M. R.; Bartell, L.; Neuhauser, D. Modeling molecular effects on plasmon transport: Silver nanoparticles with tartrazine. *J. Chem. Phys.* **2011**, *134*, 084101.
- (32) Nascimento, D. R.; DePrince III, A. E. Modeling molecule-plasmon interactions using quantized radiation fields within time-dependent electronic structure theory. *J. Chem. Phys.* **2015**, *143*, 214104.
- (33) Zhang, W.; Govorov, A. O.; Bryant, G. W. Semiconductor-metal nanoparticle molecules: Hybrid excitons and the nonlinear Fano effect. *Phys. Rev. Lett.* **2006**, *97*, 146804.
- (34) Karam, T. E.; Haber, L. H. Molecular adsorption and resonance coupling at the colloidal gold nanoparticle interface. *J. Phys. Chem. C* **2013**, *118*, 642–649.
- (35) Bigelow, N. W.; Vashillo, A.; Camden, J. P.; Masiello, D. J. Signatures of Fano interferences in the electron energy loss spectroscopy and cathodoluminescence of symmetry-broken nanorod dimers. *ACS Nano* **2013**, *7*, 4511–4519.
- (36) McMahon, J. M.; Henzie, J.; Odom, T. W.; Schatz, G. C.; Gray, S. K. Tailoring the sensing capabilities of nanohole arrays in gold films with Rayleigh anomaly-surface plasmon polaritons. *Opt. Express* **2007**, *15*, 18119–18129.
- (37) Hao, Q.; Juluri, B. K.; Zheng, Y. B.; Wang, B.; Chiang, I.-K.; Jensen, L.; Crespi, V.; Eklund, P. C.; Huang, T. J. Effects of intrinsic fano interference on surface enhanced raman spectroscopy: comparison between platinum and gold. *J. Phys. Chem. C* **2010**, *114*, 18059–18066.

- (38) Rodarte, A. L.; Tao, A. R. Plasmon–Exciton Coupling between Metallic Nanoparticles and Dye Monomers. *J. Phys. Chem. C* **2017**, *121*, 3496–3502.
- (39) Neuhauser, D.; Lopata, K. Molecular nanopolaritonics: Cross manipulation of near-field plasmons and molecules. I. Theory and application to junction control. *J. Chem. Phys.* **2007**, *127*, 154715.
- (40) Lopata, K.; Neuhauser, D. Multiscale Maxwell–Schrödinger modeling: A split field finite-difference time-domain approach to molecular nanopolaritonics. *J. Chem. Phys.* **2009**, *130*, 104707.
- (41) Corni, S.; Tomasi, J. Excitation energies of a molecule close to a metal surface. *J. Chem. Phys.* **2002**, *117*, 7266–7278.
- (42) Swathi, R.; Sebastian, K. Resonance energy transfer from a fluorescent dye molecule to plasmon and electron-hole excitations of a metal nanoparticle. *J. Chem. Phys.* **2007**, *126*, 234701.
- (43) Deinega, A.; Seideman, T. Self-interaction-free approaches for self-consistent solution of the Maxwell-Liouville equations. *Phys. Rev. A* **2014**, *89*, 022501.
- (44) Yee, K. S. Numerical solution of initial boundary value problems involving Maxwell’s equations in isotropic media. *IEEE T. Antenn. Propag.* **1966**, *14*, 302–307.
- (45) Merewether, D.; Fisher, R.; Smith, F. On implementing a numeric Huygen’s source scheme in a finite difference program to illuminate scattering bodies. *IEEE Transactions on Nuclear Science* **1980**, *27*, 1829–1833.
- (46) Mur, G. Absorbing boundary conditions for the finite-difference approximation of the time-domain electromagnetic-field equations. *IEEE T. Electromagn. C.* **1981**, 377–382.
- (47) Umashankar, K.; Taflove, A. A novel method to analyze electromagnetic scattering of complex objects. *IEEE T. Electromagn. C.* **1982**, 397–405.

- (48) Taflove, A.; Umashankar, K. Radar cross section of general three-dimensional scatterers. *IEEE T. Electromagn. C.* **1983**, 433–440.
- (49) van der Zwan, G. Derivation of the Redfield relaxation equation. 2014; https://www.researchgate.net/profile/Gert_Van_der_Zwan2/publication/260399968_Derivation_of_the_Redfield_relaxation_equation/links/0f317531467196646d000000.pdf.
- (50) Castro, A.; Marques, M. A.; Rubio, A. Propagators for the time-dependent Kohn–Sham equations. *J. Chem. Phys.* **2004**, *121*, 3425–3433.
- (51) Lopata, K.; Govind, N. Modeling fast electron dynamics with real-time time-dependent density functional theory: Application to small molecules and chromophores. *J. Chem Theory Comp.* **2011**, *7*, 1344–1355.
- (52) Yuan, X.; Borup, D.; Wiskin, J.; Berggren, M.; Johnson, S. Simulation of acoustic wave propagation in dispersive media with relaxation losses by using FDTD method with PML absorbing boundary condition. *IEEE T. Ultrason. Ferr.* **1999**, *46*, 14–23.
- (53) Taflove, A.; Hagness, S. C. *Computational electrodynamics*; Artech house, 2005.
- (54) Coomar, A.; Arntsen, C.; Lopata, K. A.; Pistinner, S.; Neuhauser, D. Near-field: A finite-difference time-dependent method for simulation of electrodynamics on small scales. *J. Chem. Phys.* **2011**, *135*, 084121.
- (55) Clapp, A. R.; Medintz, I. L.; Mattoussi, H. Förster resonance energy transfer investigations using quantum-dot fluorophores. *ChemPhysChem* **2006**, *7*, 47–57.
- (56) Wolber, P.; Hudson, B. An analytic solution to the Förster energy transfer problem in two dimensions. *Biophys. J.* **1979**, *28*, 197–210.
- (57) Govorov, A. O.; Lee, J.; Kotov, N. A. Theory of plasmon-enhanced Förster energy transfer in optically excited semiconductor and metal nanoparticles. *Phys. Rev. B* **2007**, *76*, 125308.

- (58) Kulander, K. C. Time-dependent Hartree-Fock theory of multiphoton ionization: Helium. *Phys. Rev. A* **1987**, *36*, 2726–2738.
- (59) Li, X.; Smith, S. M.; Markevitch, A. N.; Romanov, D. A.; Levis, R. J.; Schlegel, H. B. A time-dependent Hartree-Fock approach for studying the electronic optical response of molecules in intense fields. *Phys. Chem. Chem. Phys.* **2005**, *7*, 233–239.
- (60) Isborn, C. M.; Li, X. Singlet- Triplet Transitions in Real-Time Time-Dependent Hartree- Fock/Density Functional Theory. *J. Chem. Theory Comput.* **2009**, *5*, 2415–2419.
- (61) Yabana, K.; Bertsch, G. F. Time-dependent local-density approximation in real time. *Phys. Rev. B* **1996**, *54*, 4484–4487.
- (62) Andrade, X.; Strubbe, D.; De Giovannini, U.; Larsen, A. H.; Oliveira, M. J. T.; Alberdi-Rodriguez, J.; Varas, A.; Theophilou, I.; Helbig, N.; Verstraete, M. J. et al. Real-space grids and the Octopus code as tools for the development of new simulation approaches for electronic systems. *Phys. Chem. Chem. Phys.* **2015**, *17*, 31371–31396.
- (63) Meng, S.; Kaxiras, E. Real-time, local basis-set implementation of time-dependent density functional theory for excited state dynamics simulations. *J. Chem. Phys.* **2008**, *129*, 054110.
- (64) Provorse, M. R.; Isborn, C. M. Electron dynamics with real-time time-dependent density functional theory. *Int. J. of Quant. Chem.* **2016**, *116*, 739–749.
- (65) Krause, P.; Klamroth, T.; Saalfrank, P. Time-dependent configuration-interaction calculations of laser-pulse-driven many-electron dynamics: Controlled dipole switching in lithium cyanide. *J. Chem. Phys.* **2005**, *123*, 074105.
- (66) DePrince, A. E.; Pelton, M.; Guest, J. R.; Gray, S. K. Emergence of Excited-State Plas-

- mon Modes in Linear Hydrogen Chains from Time-Dependent Quantum Mechanical Methods. *Phys. Rev. Lett.* **2011**, *107*, 196806.
- (67) Huber, C.; Klamroth, T. Explicitly time-dependent coupled cluster singles doubles calculations of laser-driven many-electron dynamics. *J. Chem. Phys.* **2011**, *134*, 054113.
- (68) Kvaal, S. Ab initio quantum dynamics using coupled-cluster. *J. Chem. Phys.* **2012**, *136*, 194109.
- (69) Jeffcoat, D. B.; DePrince III, A. E. N-representability-driven reconstruction of the two-electron reduced-density matrix for a real-time time-dependent electronic structure method. *J. Chem. Phys.* **2014**, *141*, 214104.
- (70) Wall, M. R.; Neuhauser, D. Extraction, through filter-diagonalization, of general quantum eigenvalues or classical normal mode frequencies from a small number of residues or a short-time segment of a signal. I. Theory and application to a quantum-dynamics model. *J. Chem. Phys.* **1995**, *102*, 8011–8022.
- (71) Wang, F.; Yam, C. Y.; Chen, G.; Fan, K. Density matrix based time-dependent density functional theory and the solution of its linear response in real time domain. *J. Chem. Phys.* **2007**, *126*, 134104.
- (72) Bruner, A.; LaMaster, D.; Lopata, K. Accelerated broadband spectra using transition dipole decomposition and Padé approximants. *J. Chem. Theory Comput.* **2016**, *12*, 3741–3750.